

# Structured Illumination Methods

Rainer Heintzmann

## INTRODUCTION

In this chapter, I discuss methods of obtaining optical section data using methods other than standard confocal microscopy. These techniques have the potential of being more **light efficient**, **faster**, and of providing better **resolution** than standard, unprocessed confocal microscopy.

Confocal microscopy depends on an uneven distribution of the illumination on the sample, and this is accomplished by directing the beam to a single focus that is then scanned. The resulting signal is detected pointwise (voxel-by-voxel). In other systems, the focus is multiplexed and many points are scanned by a spinning disk (Petráň *et al.*, 1968; Bewersdorf *et al.*, 1998; Andresen *et al.*, 2001; Majoul *et al.*, 2002) or by the two-dimensional regular movement of a rectangular mask (Verveer *et al.*, 1998; Egner *et al.*, 2002).

Multiplexing takes advantage of the fact that many photodetectors operate in parallel to increase data throughput. In addition, by spreading the illumination over many pixels, parallel readout avoids problems, such as singlet-state fluorescence saturation, that can limit the data rate from single-beam confocal microscopes.

Multiplexed confocal systems operating with single photon excitation (Ichihara *et al.*, 1996; Verveer *et al.*, 1998) employ a structured mask (e.g., a pattern of linear or circular holes in a opaque plane or a pattern of microlenses on a rotating disk) for generating structured illumination as well as spatially filtering the fluorescent or scattered light emitted by the sample before it reaches the detector. The confocal signal is usually obtained by integrating this spatially filtered signal on the charge-coupled device (CCD) camera.

In contrast, the structured-illumination methods discussed here are based on the acquisition of a set<sup>1</sup> of individual images at a given focus plane, each made with a different position of an illumination mask, **but made with no mask in the detection beam path**, that is, widefield detection (Fig. 13.1). The detection pinholes can then be defined computationally in order to produce a confocal-like image from this set of images (as performed in Fig. 13.4). Other ways of processing the data to yield optically sectioned images are also presented below.

Some advantages and disadvantages of this strategy are:

1. Because a full image<sup>2</sup> is recorded for each position of the illumination mask, a much larger amount of data needs to be acquired per reconstructed slice. In this sense, patterned illumination with widefield detection also constitutes a “scanning” system

<sup>1</sup> A set is a series of images made at one focus plane but with different illumination conditions.

<sup>2</sup> Or at least a substantial amount of signal originating from near the positions of the illumination spots.

and sample movement must be avoided during the acquisition time. Taking multiple images can be a disadvantage in speed, but as modern CCD cameras employ fast readout systems with negligible readout noise (e.g., with electron-multiplier amplification), this does not pose a major problem.

2. This large amount of data offers more flexibility for the treatment of the data. In contrast to standard confocal microscopy, it is unnecessary to choose a pinhole diameter during data acquisition with all the advantages and disadvantages of this choice. Once you have chosen the illumination pattern, the trade-off between sectioning strength (small hole) and better signal-to-noise ratio (large hole) can be dealt with after data acquisition (see Fig. 13.4) or be avoided entirely during data processing.

3. In most structured-illumination systems, the multi-spot approach distributes the power of the illumination light across multiple positions. In a single-spot confocal system, fluorescence saturation fundamentally limits the amount of collectable fluorescent light one can excite per unit/time and thus defines a minimum time required for the acquisition of an adequate fluorescence image. Given illumination sources of sufficient brightness, the simultaneous utilization of one thousand spots can potentially shorten the acquisition time substantially.<sup>3</sup>

4. An advantage of standard confocal scanning systems is that the scan is relatively localized. Thus, sample movement only causes major image distortion if the feature actually being scanned moves by an amount that is large compared to the beam size. In contrast, patterned illumination systems with widefield detection require that each part of the object be stable within the limits of the achievable resolution throughout the acquisition of an entire set of raw data images.

## EXPERIMENTAL CONSIDERATIONS

For the sake of simplicity, an identical schematic setup (Fig. 13.1) will be assumed throughout this chapter. In this setup, the sample is illuminated through an illumination mask [e.g., Fig. 13.2(A–C)], which can be shifted by well-defined displacement to produce a set of regularly spaced light patterns. At each position of the illumination mask, an image of the sample is detected with a CCD camera at a conjugate image plane, usually maintaining a fixed, in-plane position with respect to the sample. The common features of all structured-illumination arrangements are that the sample is illuminated with structured light, and fluorescence or the scattered

<sup>3</sup> The amount by which the total acquisition time is shortened depends on how many images must be obtained at each plane, a factor that varies with the sparsity of the mask used.

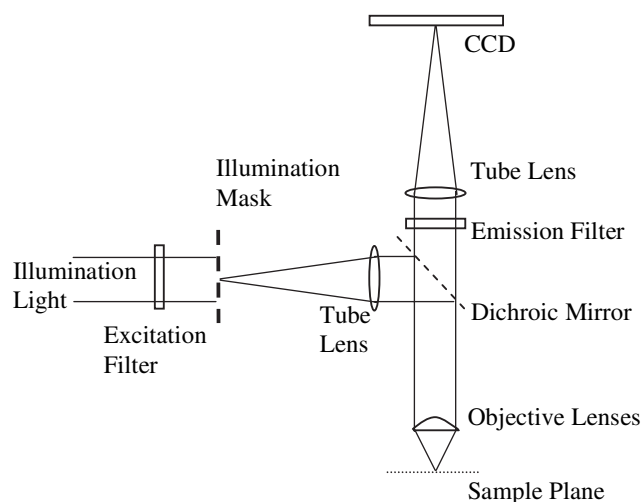


**FIGURE 13.1.** Possible experimental setup for acquiring structured-illumination data in the widefield fluorescence detection mode. The illumination mask is projected by the microscope optics onto the specimen in the sample plane, thereby defining the illumination pattern. The fluorescence light from the sample is, however, directly imaged onto the CCD camera without any mask in the detection path.

light is detected in a widefield-type arrangement without the use of any detection mask. The various structured-illumination methods differ greatly in how the pattern of light is generated (e.g., by interference patterns or even using a single-spot laser illumination) and also in the detection system [e.g., either widefield or de-scanning with detection of a small area near the illumination spot (Bertero *et al.*, 1984; Bertero *et al.*, 1989; Sheppard and Cogswell, 1990; Pawley *et al.*, 1996)]. Below, I describe different pattern generation techniques along with possible sources of errors.

## Pattern Generation

Patterns of illumination can be generated by placing the illumination mask at the plane of the field stop in the illumination path of the microscope (Fig. 13.1). The mask can be a diffraction grating, or a spatial light modulator (SLM) such as a programmable liquid crystal, a digital mirror, or a liquid-crystal-on-silicon (LCOS) device, and can be illuminated either by incoherent light (Neil *et al.*, 1997; Heintzmann and Cremer, 1999a) or by a coherent laser (e.g., as in Lanni *et al.*, 1993 or Gustafsson, 2000).

For the optimal signal-to-noise ratio at the highest in-plane resolution, it is advantageous to produce the highest possible contrast (degree of modulation) of the light pattern in the sample plane. The

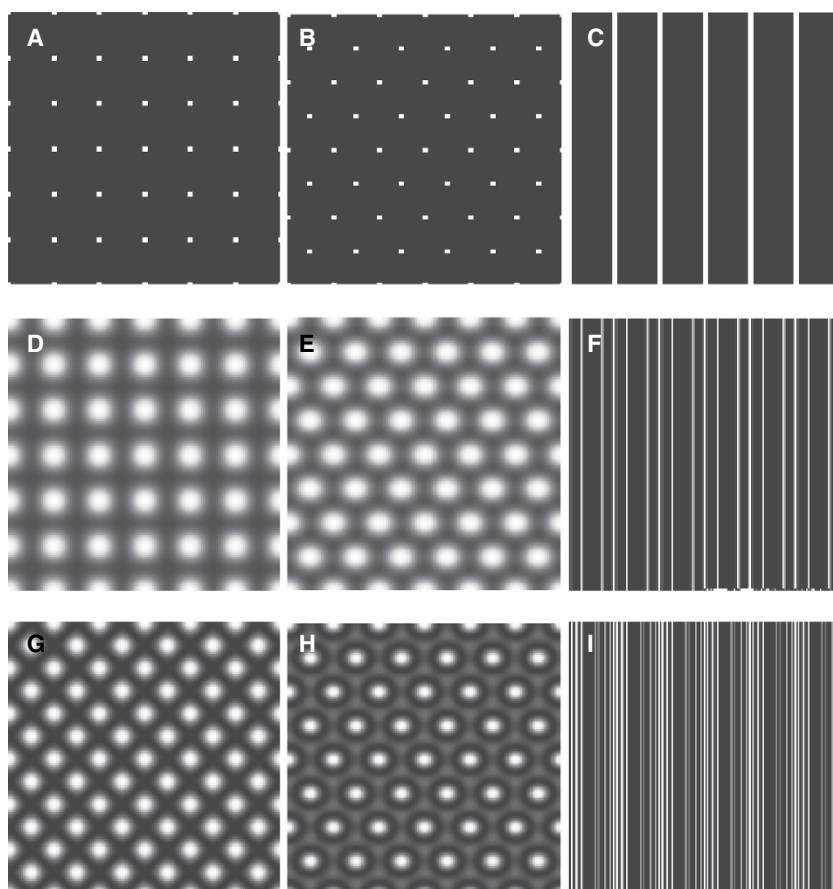


**FIGURE 13.2.** Different pattern masks (top row) along with the illumination patterns (rows below) generated in the plane of focus. (A) Regular spaced dots; (B) illumination dots placed on a hexagonal unit cell such as often used in spinning disk systems; (C) Line-grid. The unit-cell length  $D$  is indicated. (D–F) show the illumination pattern as generated by incoherent imaging of (A–C) at the sample plane. (G–I) correspond to coherent imaging with suppression of the zero-order in the diffraction pattern. Note the improved degree of modulation, yielding a darker background.

light diffracted from a coherently illuminated grid can be focused to well-defined diffraction orders. To achieve the maximum degree of modulation, it can be advantageous to block the zero diffraction order (stemming from non-diffracted light) with the help of a central beam stop at an appropriate position in the illumination path. It is also possible to generate illumination patterns by interfering beams of coherent light that have been separated by beam-splitters (Lanni *et al.*, 1986; Lanni *et al.*, 1993; Frohn *et al.*, 2000). However, in this case mechanical stability becomes a major concern because the relative length of the two beam paths formed by the splitter must remain stable to subwavelength precision during the time needed to record an entire set of images.

When working with microscopes that possess high aperture angles in the sample plane, it is important to keep the vector nature of light in mind (Fig. 13.3). Beams converging onto the focus plane at an angle of  $90^\circ$  with respect to each other do not generate an intensity interference pattern in *p*-polarization (meaning the polarization vector is in the plane defined by the two interfering beams), whereas the interference of *s*-polarized beams (polarization vector perpendicular to the plane that contains the two interfering beams) results in optimum mask contrast.<sup>4</sup> At a high numerical aperture, this consideration makes line-grid diffraction masks [e.g., Fig. 13.2(C)] with *s*-polarized illumination (polarization vector parallel to the lines) preferable to two-dimensionally structured masks.

The ideal source of this light is less clear. Because laser light is both polarized and very bright, it may seem an obvious choice. If a grating or SLM is used to generate an array of lines, the zero-order, undiffracted beam can be easily discriminated and removed to achieve the maximum possible modulation at the focus plane. Furthermore, laser light can be coupled into the microscope very efficiently even at high diffraction angles and, in combination with holographic techniques, it can be used to generate sparse patterns without a severe loss in total power. However, at present, laser light is only available at certain wavelengths and these do not always match the absorption spectra of the dyes of choice. In addition, the high lateral coherence of laser light can cause strong interference effects between the main beams generating the structure and light reflected by various optical surfaces, particularly the water–glass

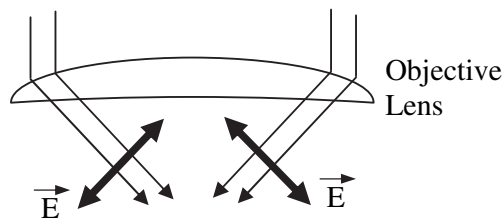


**FIGURE 13.3.** Influence of the vector nature (polarization/electric field) of light at high numerical aperture. The interfering electric field vectors (*bold arrows*) perpendicular to the light rays (*thin arrows*) can even be perpendicular to each other at *p*-polarization, and an aperture half-angle of  $45^\circ$ , as displayed here, leads to no intensity modulation in the sample plane. In contrast, *s*-polarization with the electric field vector pointing towards the reader would yield two parallel vectors and thus 100% contrast in the intensity pattern generated by constructive and destructive interference.

<sup>4</sup> Whereas *p*-polarized rays that converge at a relative angle of  $40^\circ$  are still capable of interfering well enough to produce 90% of full contrast.

surfaces of the coverslip and the front surface of any non-immersion objective. Although lateral coherence can be scrambled in a number of ways (as discussed in Chapter 6, *this volume*), implementing these strategies adds so much complexity and cost that they have so far been used only in homemade systems.

Arc sources usually are less expensive, less coherent, and much less bright than laser sources (see Chapter 6, *this volume*). However, they emit over a very wide range of wavelengths and, particularly at the peaks of the Hg emission lines, they are bright enough for many studies. Because arcs can be considered as longitudinally and transversally incoherent, stray interference fringes are seldom a factor.

Their problem is insufficient brightness. If the illumination system is adjusted so that it only uses the light emerging from a small area of the source, the blocking of the zero order would still be possible. However, doing so reduces the intensity so much that long exposures are needed to maintain a decent signal-to-noise ratio in each image in the data set. To make matters worse, sparse illumination patterns can obstruct more than 90% of the incident light striking the pattern mask. Finally, as sheet polarizers transmit only about one third of the incident light, it is a matter of some interest as to whether or not, given a fixed exposure time, the increased contrast of the pattern is offset by the lower signal level caused by the use of the polarizer. As a rule of thumb, unless it is essential to collect data very rapidly, the  $3\times$  lower illumination intensity that occurs when you use a sheet polarizer is recommended for aqueous specimens whenever the objective numerical aperture (NA) is  $>0.4$ , using high spatial frequency gratings for in-plane resolution enhancement, or  $>0.8$ , when using lower spatial frequency gratings for optical-sectioning applications.

On the other hand, if one uses an arc source to project a pattern large enough so that its image is only marginally affected by diffraction, one can use an illumination system that utilizes light from a larger area of the source and the photon flux becomes sufficient for rapid optical sectioning using patterned illumination. Indeed, the Zeiss ApoTome is such a device. In the future, it may be possible to use an array of high-power, light-emitting diodes (LEDs) as a bright, incoherent source of patterned illumination.

The choice of the illumination pattern density very much depends on the type of sample as well as on the intended method of data processing. A comparably thick sample and/or a sample with volume-like staining is more difficult to process when using densely patterned illumination because the large amount of out-of-focus fluorescence will dominate the small amount of modulated fluorescence stemming from the focal plane (see Appendix, *this chapter*). Although using a sparse pattern reduces this signal-to-noise problem, it always requires the acquisition of more raw data images to produce a single set. This implies a longer image acquisition time. An elegant way to achieve sufficient flexibility and to optimize this trade-off between relatively noise-free sectioning and acquisition speed is to generate the pattern using a programmable array (Verveer *et al.*, 1998; Hanley *et al.*, 1999; Heintzmann *et al.*, 2001; Fukano and Miyawaki, 2003).

Out-of-focus-light can be reduced by closing the field diaphragm (Hiraoka *et al.*, 1990) and this technique may be very valuable. However, when using non-local reconstruction methods (e.g., the Fourier-space based approaches) the illumination pattern is assumed to be periodic at all out-of-focus positions. A small field diaphragm violates this assumption and may lead to problems during Fourier-based reconstruction.

The illumination pattern can be displaced relative to the sample by either translating the mask by a well-defined distance (Neil *et al.*, 1997; Gustafsson, 2000, 2005), by reprogramming the

pattern of a programmable diffraction (amplitude or phase) mask (Verveer *et al.*, 1998; Hanley *et al.*, 1999; Heintzmann *et al.*, 2001; Fukano and Miyawaki, 2003), by altering the relative phases of interfering beams (e.g., by splitting the beam and repositioning a piezo-actuated mirror in one of the beam paths) (Lanni *et al.*, 1993; Frohn *et al.*, 2000; Failla *et al.*, 2002), or by translating the sample past a fixed pattern, followed by a computational correction to account for this sample movement (Heintzmann and Cremer, 1999a). In the latter case appropriate interpolation kernels or Fourier-space based resampling approaches (leading to a sinc kernel) must be used to reduce interpolation-induced artifacts (Yaroslavsky, 2003) that occur as features on the object move across the pixels of the CCD.

Promising attempts to replace the confocal pinhole by a multiple element detector (Bertero *et al.*, 1984; Barth and Stelzer, 1994) with fast readout (Sheppard and Cogswell, 1990; Pawley *et al.*, 1996) also belong to the same category of structured illumination with somewhat widefield-like detection.<sup>5</sup> The data can thus be treated with methods similar to the descriptions given below, as long as the descanning is accounted for.

## COMPUTING OPTICAL SECTIONS FROM STRUCTURED-ILLUMINATION DATA

The data acquired with a setup similar to the one shown in Figure 13.1 consists of a  $z$ -series of sets of images. Each set is taken at one focus position and each member of a set is taken at a different position of the illumination light pattern. The data from each set is first processed to yield an optically sectioned image using one of the methods described below.

Most methods for deriving an optical section from a set of structured-illumination images try to estimate the **degree of modulation** at each pixel. For simplicity, in the case of a one-dimensional grid [e.g., Fig. 13.2(C), top row in Fig. 13.7, p. 272, Fig. 13.11, p. 278] it is assumed that  $N$  images are acquired, each with the pattern shifted by  $1/N$  with respect to the replicative unit cell.<sup>6</sup> In the top row of Figure 13.7, the interleaved positions of the three illumination patterns are indicated on the left side of each image for  $N = 3$ . As displayed in Figure 13.11, those parts of the sample that are out of focus are more homogeneously illuminated. Light emitted from these parts will undergo an additional blurring when imaged onto a detector conjugate to the in-focus plane. Thus, in contrast to the in-focus light, light from out-of-focus areas will exhibit very little modulation upon variation of the  $x$ -positions of the excitation pattern. Computing the degree of modulation over the multiple images, in a pixel-by-pixel fashion, will permit the discrimination of the non-modulated, out-of-focus from the modulated, in-focus information.

The degree of modulation can be calculated **locally**, considering only the modulation at a single pixel position over time, by various approaches:

1. Dodt (Dodt, 1990; Dodt and Becker, 2003) suggests emulating “synthetic pinholes” by summing up the thresholded images

of a series of data acquired by transmission imaging with structured illumination. This technique has been successfully applied to the transmission infrared (IR) imaging of onion skin (Dodt and Becker, 2003) and 300  $\mu\text{m}$  unstained, freshly prepared thick rat hippocampal slices in which single spines on dendrites could be resolved throughout the sample (40 $\times$ , NA 0.8 objective at 780 nm, Dodt *et al.*, 2001). The advantage of this approach is that, while the optical aberrations induced by such samples render the operation of a standard confocal microscope in transmission close to impossible, the data processing strategy employed is very adaptive to optical aberrations and thus is able to yield a useful image containing information mainly from the focal slice.

2. Benedetti and co-workers (Benedetti *et al.*, 1996) determined the reconstructed slice  $I_{\text{rec}}$  by calculating the difference between maximum and minimum measured intensity  $I_i$  in each pixel  $i$ : [Eq. 1, see also Fig. 13.7(B)]. This approach<sup>7</sup> is robust with respect to various artifacts that often arise in imaging such as readout noise and especially fixed-pattern noise from the CCD. This noise, which usually does not vary systematically over time but rather randomly from pixel to pixel, is efficiently eliminated, as is scattered light from out-of-focus planes and from anywhere in the optical path. It is observed that this approach generates spurious patterns if the number of scanning steps is too low for the size of the illumination pattern as is seen by the residual horizontal stripes visible in Figure 13.7(B). However, it should be noted that the selected width for this pattern was extraordinarily wide and only three steps were chosen. For a denser pattern or an increased number of scanning steps, the visible performance of this method is similar to approach 3 [Fig. 13.7(C)], which is discussed below.

If the illumination pattern is sufficiently sparse [i.e., the spot-to-spot or line-to-line distance  $D$  in Figure 13.2(C) is large enough or, more generally, if the ratio of open to opaque area, the so-called mark/space ratio, is low], simply computing the maximum (Eq. 2) yields fairly good optical sections (Benedetti *et al.*, 1996), albeit without the background suppression advantages of Eq. 1. These approaches have been applied to epi-fluorescence microscopy (Benedetti *et al.*, 1996) and transmission IR imaging (Dodt and Becker, 2003). By Eq. 3 (termed super-confocal), a further increase in optical sectioning quality is obtained. However, Eqs. 2 and 3 yield satisfying results only for data acquired using sparse illumination.

3. Other ways of determining the degree of modulation (Eqs. 4, 5) are described by Neil (Neil *et al.*, 1997). Equation 4 is based on square-law detection [Fig. 13.7(C)] and Eq. 5 emulates a homodyne detection scheme. Another possible approach is the computation of the absolute magnitude of the pixel-by-pixel Fourier-transform over each set of images (Ben-Levy and Peleg, 1995). For the case of three such images, this method is identical to Eq. 5. It should be noted that both of these methods would not be able to reconstruct the high  $xy$ -spatial frequency given in the moiré example discussed later [Fig. 13.5(A)], in which the Fourier-transform of the illumination grid has its peaks just outside the range of detectable spatial frequencies. This is the case when the highest possible fluorescent excitation spatial frequency is passed through the objective. Such light will consist of two beams passing through the edges of the back-focal plane. Because of the Stokes shift of the excited fluorescence light, this spatial frequency will

<sup>5</sup> For speed reasons, the suggested detector arrays are usually relatively small (e.g.,  $5 \times 5$  elements), yielding a confocal operation “bias” for thick specimens.

<sup>6</sup> The unit cell is defined as the smallest (vectorial) translation that can be applied to the pattern to reproduce its structure (e.g., the distance  $D$  indicated in C, Fig. 13.2).

<sup>7</sup> A system (ViCo) based on this and related concepts is marketed by Biomedica Mangoni s.n.c., Pisa, Italy.

not be imaged by the objective on the return trip. A similar situation occurs when employing grazing incidence illumination as in Frohn and colleagues (2000). Most strategies assume equally distributed phases between the images, but this is not a strict requirement. Fukano and Miyawaki (Fukano and Miyawaki, 2003) use a three-phase scheme with a relative phase of  $2\pi/4$  between the three images, and a modified Eq. 4 for sectioning. With unequal phase approaches, care has to be taken (e.g., by shifting the 0-phase between series of images) to avoid bleaching illumination structure into the sample over time.

4. Scaled subtraction of the background is yet another way to process the raw images. Assuming that the nominal position and width of the illumination pattern is known, a pixel at the plane of focus is either illuminated or not in each of the images. First

1. 
$$I_{rec}(x,y) = \text{Max}_{n=0\dots N} I_n(x,y) - \text{Min}_{n=0\dots N} I_n(x,y)$$
2. 
$$I_{rec}(x,y) = \text{Max}_{n=0\dots N} I_n(x,y)$$
3. 
$$I_{rec}(x,y) = \text{Max}_{n=0\dots N} I_n(x,y) + \text{Min}_{n=0\dots N} I_n(x,y) - 2\text{Avg}_{n=0\dots N} I_n(x,y)$$
4. 
$$I_{rec}(x,y) = \sqrt{\sum_{n=0}^N (I_n(x,y) - I_{(n+N \text{ div } 2) \bmod N}(x,y))^2}$$
5. 
$$I_{rec}(x,y) = \left| \sum_{n=0}^N I_n(x,y) \exp(2\pi i n / N) \right|$$
- 6a. 
$$I_{rec}(x,y) = \sum_{n=0}^N I_n(x,y) \text{Mask}_n^{\text{on}}(x,y) - \gamma \sum_{n=0}^N I_n(x,y) \text{Mask}_n^{\text{off}}(x,y)$$
  

$$\gamma = \frac{1}{\text{MAR}} - 1$$
- 6b. 
$$I_{rec}(x,y) = \beta \left[ \frac{\sum_{n=0}^N I_n(x,y) \text{Mask}_n^{\text{on}}(x,y)}{\sum_{n=0}^N \text{Mask}_n^{\text{on}}(x,y)} - \frac{\sum_{n=0}^N I_n(x,y) \text{Mask}_n^{\text{off}}(x,y)}{\sum_{n=0}^N \text{Mask}_n^{\text{off}}(x,y)} \right]$$
  

$$\beta = \frac{N \sum_{n=0}^N \text{Mask}_n^{\text{on}}(x,y) - \left[ \sum_{n=0}^N \text{Mask}_n^{\text{on}}(x,y) \right]^2}{N \sum_{n=0}^N (\text{Mask}_n^{\text{on}}(x,y))^2 - \left[ \sum_{n=0}^N \text{Mask}_n^{\text{on}}(x,y) \right]^2}$$
- 7a. 
$$\tilde{I}_{rec}(\vec{k}) = \frac{\sum_{l=-m}^m \alpha_l \tilde{\rho}_l(\vec{k} - \vec{s}_l)}{\sum_{l=-m}^m \frac{1}{(\sigma_l \alpha_l)^2}}, \quad \alpha_l = \frac{\tilde{h}_{goal}(\vec{k})}{\tilde{h}_{em,l}(\vec{k} + \vec{s}_l)}$$
- 7b. 
$$\tilde{\rho}_l(\vec{k}) = \sum_n (M^{-1})_{nl} \tilde{I}_n(\vec{k})$$

$n$ : index of the acquired images (the grid position varies with  $n$ )  
 $N$ : number of acquired images,  $x,y$ : in-plane positions in the image  
 $i$ : imaginary constant,  $l$ : indexing the components (separated order)  
 Max, Min, Avg: respective maximum, minimum or average value, computed at each pixel over all  $N$  successively acquired images.  
 $\text{Mask}_n^{\text{on}}$  and  $\text{Mask}_n^{\text{off}} = 1 - \text{Mask}_n^{\text{on}}$  define which pixel was illuminated or not illuminated in a given frame  $n$   
 $\text{MAR}$  is the mark/area ratio describing the fraction of pixels considered to be illuminated

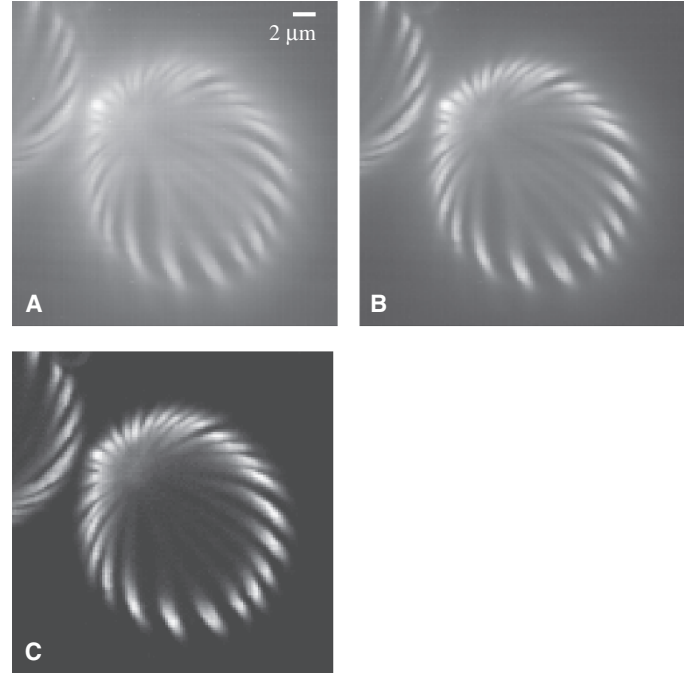


**FIGURE 13.4.** Confocal slices computed from structured-illumination data. (A) Virtual pinhole diameter chosen to be half the spot-to-spot distance. (B) Virtual pinhole selected as 0.15 of the spot-to-spot distance. (C) Scaled subtraction method with fixed  $\beta = 1$  (see Eq. 6 in boxed list of equations) and illumination spot of Gaussian shape with width as in (B). [The experimental data for this figure was kindly provided by Pier Alberto Benedetti (pollen grain taken at 1.3 NA, ~450 nm excitation, ~550 nm emission,  $6 \times 6 = 36$  patterned images acquired for this single slice, 200 nm pixel pitch in sample, spot-to-spot distance, 2.1 μm in sample).]

the value of each pixel is averaged over multiple images, each recorded at one of the positions of the illumination structure, that illuminates the in-focus parts of the sample in this pixel (ON). A second average is taken of all the pixel values where the pixel is nominally not irradiated (OFF) and subtracted from the first ON average. This technique estimates and removes the pinhole-to-pinhole background fluorescence, assuming that in-focus parts of the object do not yield fluorescence when not irradiated and out-of-focus parts fluoresce with equal brightness independent of the position of the illumination structure. It is termed “scaled subtraction” because only a scaled fraction of the sum of the pixel intensities in the non-illuminating frames has to be subtracted from the sum in the illuminating frames. Such a technique is commonly used for data where only these sums are acquired (conjugate and non-conjugate light) as in the programmable array microscope (Hanley *et al.*, 1999; Heintzmann *et al.*, 2001). The method and the scaling factor  $\gamma$  that is applied to the non-illuminated sum is covered by Eq. 6. Theoretically, such a scaled subtraction may yield negative results even in the totally noise-free limit, but these are so small that they can be neglected in practice. Note that even though  $\text{Mask}^{\text{ON}}$  and  $\text{Mask}^{\text{OFF}}$  in Eq. 6 were initially thought of as being binary masks, this technique of scaled subtraction can also be used with smooth masks [see Eq. 6(b)], in which case the binary mask is replaced by the spatially varying excitation probability in the computation. Equation 6(b) has been constructed in such a way that small spatial variations in mask intensity (e.g., due to moiré effects) are accounted for. If this is not an issue,  $\beta$  can be set to 1. The effect of Eq. 6(b) with  $\beta$  fixed to 1, is shown in Figure 13.4(C).

Note that, in contrast to filtering approaches, which consider information in neighboring pixels, this processing considers the multi-frame data pixel by pixel. The optical sectioning visible in Figure 13.4 can thus not be explained as being the effect of a high-pass filter applied to the image data. It is a genuine method of optical sectioning obtained by processing images made at multiple illumination positions.

The scaled subtraction approach has also been used in a slightly different context of aperture correlation microscopy (Wilson *et al.*, 1996). In the first image, a mask with holes at random positions in it is scanned over the object and the image through the same mask is acquired. The second image consists of a, usually shorter, exposure with widefield illumination. Scaled subtraction of the two images serves to remove the remaining widefield information, which is present in the image acquired with illumination and detection through the random mask. A similar, yet more signal-to-noise effective approach, obviating the need for a separate widefield image, is to image the light rejected at the mask onto a separate detector (Hanley *et al.*, 1999; Heintzmann *et al.*, 2002) and also process the data by scaled subtraction.

All of the above techniques process the data **locally** by considering only a single pixel position in all the members of an image set for its own reconstruction and ignoring the intensities of neighboring pixels. Some of the above methods (Eqs. 1–5) are **non-linear** in the sense that, during reconstruction, they employ at least one nonlinear operation such as thresholding, squaring, computing the absolute magnitude, or the maximum. In the absence of noise, they do remain linear with respect to the emitted light intensity. As long as the signal-to-noise ratio is high, the deviations from a linear treatment remains negligible and the resulting images can be used for quantification. However, in low-signal situations (e.g., high out-of-focus background) the deviation of the output from the true intensities in the sample will be severe. The nonlinear steps (absolute value, square root, maximum, minimum) statistically bias the result due to the influence of the noise, for example, when the true degree of modulation in a pixel should be zero but a high background is present in each of the images, methods based on taking the absolute value (Eqs. 4, 5) will yield a positive result just from the noise. They will not yield zero on average, whereas a linear method would be expected to do so.

The above evaluation techniques have the advantage of being fast and easy to compute. They do not require any knowledge of the absolute pattern position nor do they need to estimate this information from the measured data. Furthermore, they often show an inherent robustness to inexact pattern positioning. However, the results they produce are generally inferior to those achievable by approaches for the linear processing of structured-illumination data as outlined below.

## RESOLUTION IMPROVEMENT BY STRUCTURED ILLUMINATION

In addition to achieving optical sectioning (Frohn *et al.*, 2001), structured illumination can also yield improved lateral resolution. The reason is that there is a moiré effect between the structured illumination pattern and the structure of the object, such that previously inaccessible spatial frequencies of the sample become detectable (Fig. 13.5). However, to yield a useful reconstruction, the illumination pattern must first be disentangled from the detected moiré fringes. This method was first conceived by Lucosz for the case of a rather dense line-grid illumination [Fig. 13.2(C)] and detection masks (Lucosz and Marchand, 1963) (the unit-cell

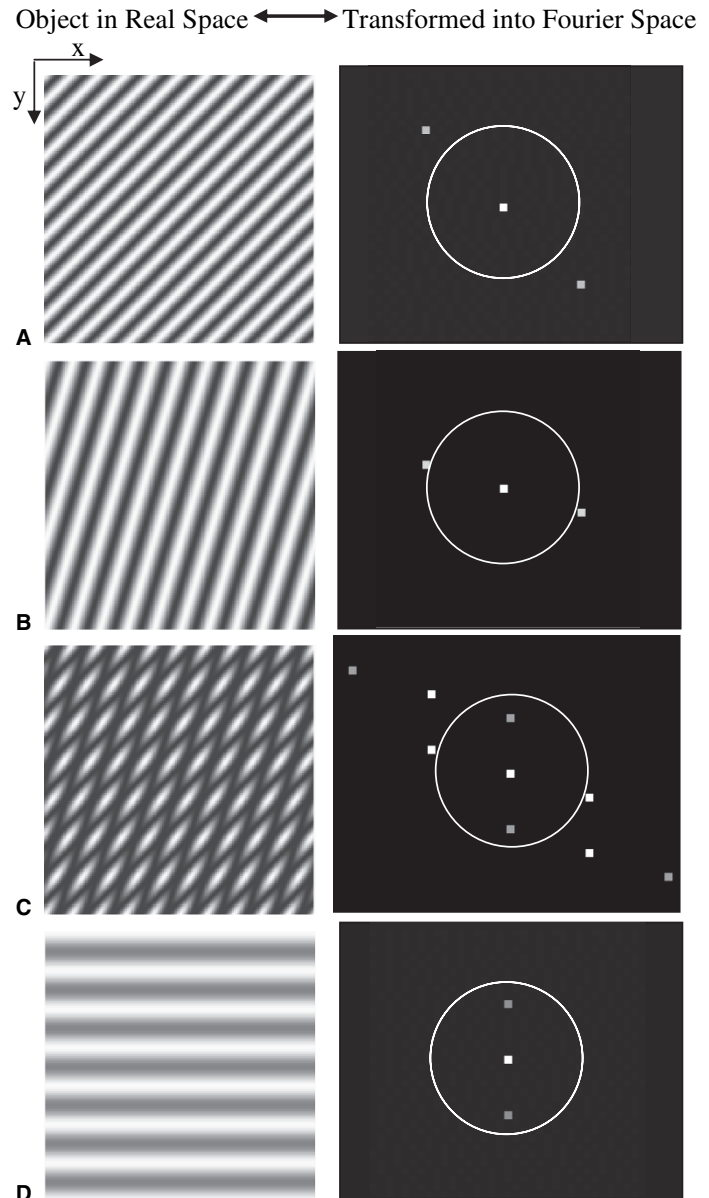


**FIGURE 13.5.** Moiré effect. A microscope can only detect information up to a maximal spatial frequency. In other words, a minimum distance between the maxima of a grid-like feature in the sample is required. The left column shows real-space features, whereas the right column shows the corresponding situation in Fourier-space. The circle indicates the limiting frequency (pass-band of the transfer function) up to which the microscope can detect information. In (A), a grid feature of the sample is shown that cannot be resolved with evenly distributed illumination, yielding equal fluorescence everywhere in the detected image. By illumination with another dense spatial grid (B), an aliased grid (C) is generated (moiré effect) that can then be partially detected (D). However, this detected grid (D) has “incorrect” spacing. Detailed knowledge about the moiré effect generated by the illumination pattern (B) can be used to reassign the detected spatial frequency to the correct place, thereby reconstructing (A).

distance in the sample coordinate system was on the order of the size of the point spread function) and also for two-dimensional grid [Fig. 13.2(A)] patterns (Lucosz, 1967). These arguments are based heavily on Fourier-space considerations and form the basis for all the computational unmixing systems used for data from widefield detectors recording images excited by structured illumination (as in Fig. 13.1).

**FOURIER-SPACE — AN INTRODUCTION**

Fourier-space is extremely useful in discussing optical imaging because the process of imaging can be modeled by simply multiplying the Fourier-transform of the sample distribution by the Fourier-transform of the point spread function of the microscope (the so-called optical transfer function); a process that is carried out in Fourier-space. To turn this result into a simulation of the image, this product must be “inverse-Fourier transformed” to bring it back into real space.

The concept of Fourier-space is based on the idea that any function in one-, two-, or three-dimensional space (e.g., a fluorophore distribution) can be represented as a sum of sinusoids varying in spatial frequency, direction, strength, and phase (position). The **spatial frequency** (or wave number) of a sine wave describes the number of bright maxima per distance (e.g., with the unit of  $\text{meter}^{-1}$ ). Its component along the  $x$ -axis is indicated by  $k_x$ , while the number of maxima counted along the  $y$ -axis is termed  $k_y$ . The right column of Figure 13.5 shows the magnitude of the Fourier-transformation of simple structures consisting of one (A, B, D) or only a small number of sine waves [Fig. 13.5(C)]. The displayed brightness is proportional to the magnitude of the transform at each location in Fourier-space (also called reciprocal space, frequency space, or  $k$  space). Such a plot shows only the strength of the sine wave, its direction, and spatial frequency. The exact phase (defining the position of the first maximum) is not displayed. The center in Fourier-space is located in the middle of each image. This position of zero spatial frequency corresponds to a uniform brightness in real space. The intensities away from the origin represent smaller and smaller spacings the farther out that they are.

As is apparent from Figure 13.5(A,B,D), a sinusoid shifted to all-positive values (by adding a constant), for example, the emitted sample intensity, yields three peaks in its Fourier-transformation. The central, zero-frequency peak represents the added constant and the two other peaks, taken together form the remaining sine wave in real space. Each individual peak in Fourier-space actually forms a complex-valued wave  $\exp(i2\pi\mathbf{k}\mathbf{r})$  with the respective  $\mathbf{k}$  vector in positive/negative directions. As a sum these constitute the sine in real space:  $2\sin(2\pi\mathbf{k}\mathbf{r})$ .

For a preliminary understanding of Fourier-space, it is sufficient to know that the values at two opposing positions in  $k$  space are complex conjugates to each other and when combined always form a sine wave in real space. Note that the small features of a sample are represented by sums of sine waves with high spatial frequency (small distance between successive wave maxima), such as is indicated in Figure 13.5(A). A coarser sinusoid [e.g., Fig. 13.5(D) as compared to Fig. 13.5(A)] has a  $\mathbf{k}$  vector closer to the origin of Fourier-space.

The process of imaging is represented as a modification of the Fourier-transform of the sample distribution caused by multiplying it by the optical transfer function in Fourier-space. This function decays smoothly and amounts to zero everywhere beyond a certain maximum spatial frequency. This position, beyond which no information can be transferred, is indicated by the white circles in Figure 13.5. The decaying optical transfer function of a widefield microscope is also indicated by the dotted line in Figure 13.6. For a widefield microscope this in-plane cut-off frequency, when translated into a peak-to-peak distance of a sinusoid corresponds to the equation  $d = \lambda/(2NA)$ , with the vacuum wavelength  $\lambda$  and the numerical aperture  $NA$ .

To properly measure a sample feature (sinusoid) of this frequency, the observer needs to measure at a pixels-to-pixel spacing of below half this distance to avoid misinterpretation (aliasing) of the result. This required maximal pixel-to-pixel distance is called the Nyquist distance  $d_{\text{Nq}} = \lambda/(4NA)$ . For a different introduction to Fourier space, see the Appendix to Chapter 24, *this volume*.

Imaging can be treated elegantly in Fourier-space (see box “Fourier-Space — An Introduction”) because a microscope essentially acts as a Fourier-filter. The periodic pattern introduced in the illumination path of the microscope yields a modification of the incident and thus of the emitted light. For fluorescence or reflection-type microscopy, the emitted light can be described as a multiplication of the sample structure times the illumination inten-

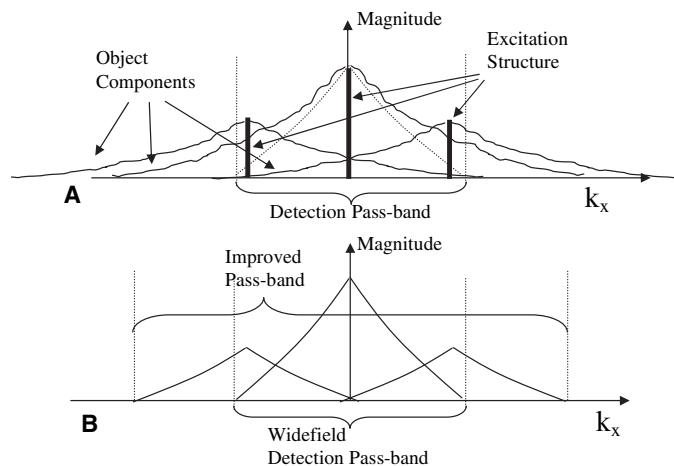


**FIGURE 13.6.** Scheme of the linear image reconstruction. (A) Fourier-transform of the structure of the emitted light. The optical transfer function defining the range of detectable special frequencies is indicated by the dotted line. (B) Detection sensitivity for the various reconstructed orders with their zero-frequency relocated to the origin.

sity or amplitude structure, respectively. This multiplication in real-space translates into a convolution in Fourier-space. Due to the periodicity of the illumination distribution, its Fourier-transform is a number of ( $\delta$ ) peaks at the reciprocal grid positions. The pattern of emitted light is a multiplication (in real space) of the illumination intensity distribution with the Fourier-transformed object, thus its Fourier-transformation is a sum of multiple Fourier-transformed objects (termed object components). These object components have their zero-frequency displaced to align with the reciprocal grating of the illumination distribution [Fig. 13.6(A), Fig. 13.8(C)]. The position and shape of the illumination structure in real space determines the individual position, strength, and phase of the multiple overlapping object components in Fourier-space.

The imaging of this emission intensity distribution is then described in Fourier-space by a multiplication with the optical transfer function. It is possible to computationally unmix the sum of the displaced copies of the object [Fig. 13.8(D)] by inversion (or pseudo-inverse) of the mixing matrix  $M$ , which mathematically describes the linear superposition of displaced object components and their relative phases [Eq. 7(b); see also Gustafsson, 2000; Heintzmann, 2003] and to shift the displaced position of their zero object frequency back to the real zero frequency. This shifting makes it obvious that, in comparison to flat-illuminated widefield microscopy, the pass-band of the microscope has then been increased by this moiré effect [Figs. 13.6(B), 13.8(E)]. Note that as opposed to the previously described methods (paragraphs 1–4), such resolution increase is even possible when the spatial modulation frequency falls outside the pass-band and is thus not imaged.

Acquiring a set of images (similar to the top row in Fig. 13.7), makes it possible to unmix the overlapping displaced object components [Fig. 13.8(C)]. An equation system for this unmixing can be constructed [Eq. 7(b)] by using the unique dependence of the complex phase of each object component on the position of the illumination structure. In a last step of image reconstruction, the individual unmixed object components [e.g., Fig. 13.8(D)] are shifted to their proper positions in Fourier-space, and multiple components that are present at the same frequency are averaged with frequency dependent weights (e.g., with the inverse variances

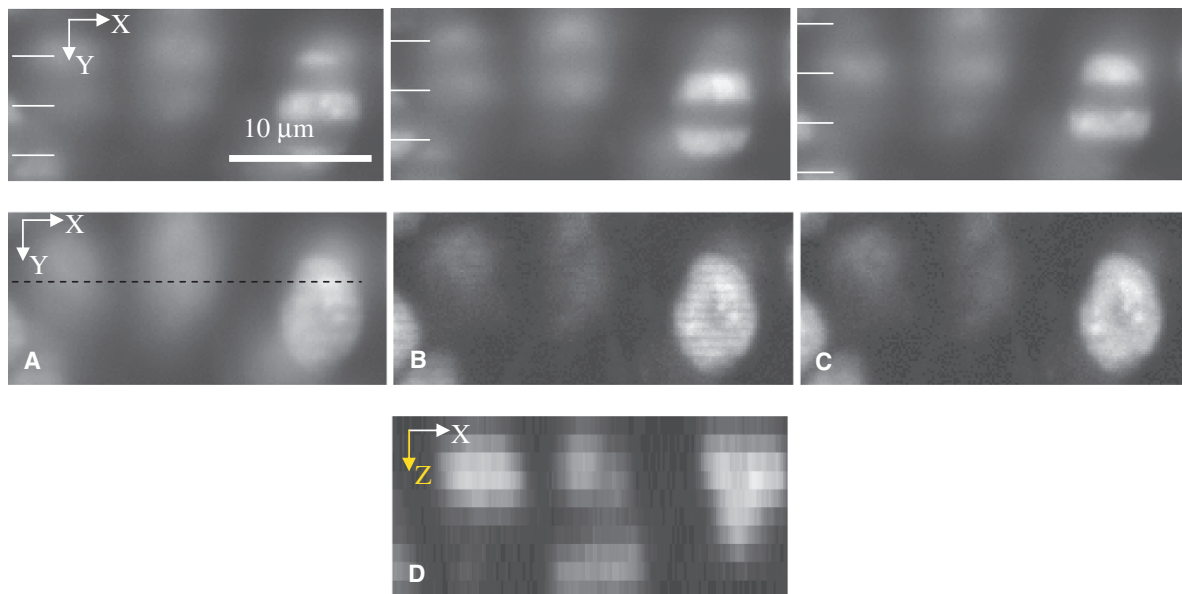


**FIGURE 13.7.** Reconstruction results obtained by different strategies. The top row shows the three individual raw data images taken at different illumination pattern positions (as indicated by the white lines at the left side of each image) with a Zeiss ApoTome setup (Axiovert,  $40\times$  NA 1.3 objective,  $\sim 3.4\mu\text{m}$  pattern pitch in the sample, AxioCam 6.7 $\mu\text{m}$  pixel pitch). The middle row shows the results obtained by (A) The sum (B) max-min, Eq. 1, (C) quadrature method, Eq. 4. Panel (D) shows an  $xz$ -cut obtained from the ApoTome software at the approximate slicing position indicated by the dashed line in panel (A). The three-dimensional sectioning capability discriminating between layers of cells is seen nicely in (B), (C), and (D).

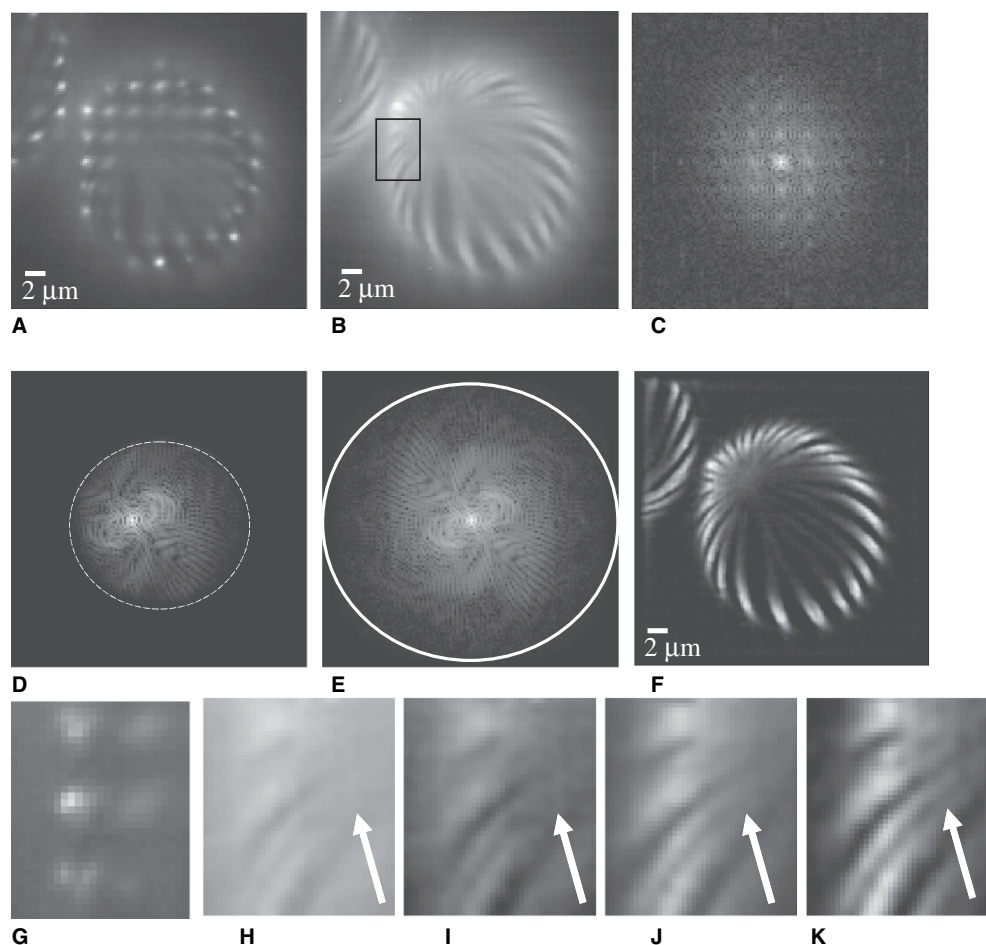


**FIGURE 13.8.** Various steps in the image reconstruction process. (A) An example raw data image. (B) The widefield image computed by summing over all partial images. The region of interest (ROI) used for images (G) to (K) is indicated as a black rectangle. (C) Magnitude of the Fourier transformation of (A), displaying the multiple overlapping components. (D) One ( $k = 1.0$ ) object component separated from multiple measurements similar to (C) taken at varying illumination mask positions [one such position is shown in panel (A)]. The region of support in detection is indicated by the dotted white circle. (E) All components shifted, averaged, and apodized (border indicated by white circle). (F) Final reconstruction result in the linear case (total of 7 orders). (G) ROI extracted from raw data shown in panel (A). (H) ROI from widefield-like image as shown in (B). (I) Image (H) contrast-enhanced. (J) Contrast-enhanced ROI from confocal processing as shown in Figure 13.4(B). (K) Equivalent zoom of image (F). [The raw data for this figure was kindly provided by Pier Alberto Benedetti (for acquisition parameters see Figure 13.4).]

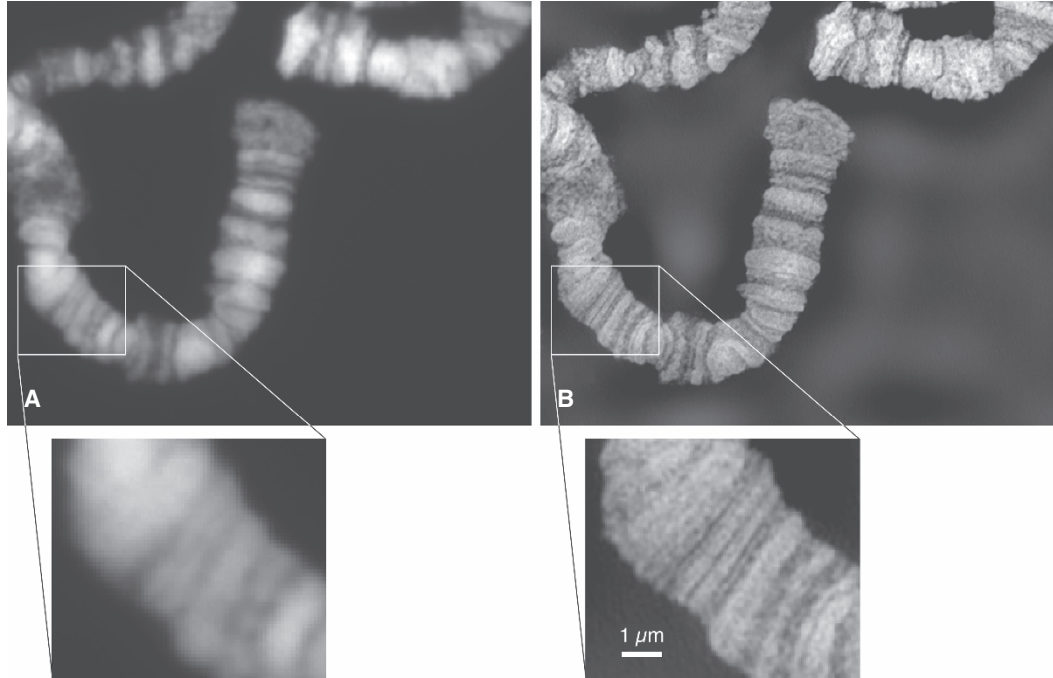


**FIGURE 13.9.** Demonstration of resolution extension by structured-illumination microscopy. The sample is a squash preparation of a polytene chromosome from a salivary gland of the fruitfly *Drosophila melanogaster*, stained for DNA with Oligreen to show the characteristic banding pattern. Many band features that are undetectable in the conventional microscope image (A) are clearly visible in the structured-illumination microscopy reconstruction (B). The structured illumination consisted of a one-directional pattern of parallel lines with a period of  $0.20\ \mu\text{m}$ , at a wavelength of  $457\ \text{nm}$ . This pattern frequency, about 80% of the resolution limit, is much higher than those used in the rest of this chapter. Nine raw data images were used: three images with a relative phase shift of  $2\pi/3$ , for each of three pattern orientations spaced  $120^\circ$  apart. The reconstruction used a Fourier-based algorithm that includes compensation for the detection OTF, as described in Gustafsson (2000). [These images were kindly provided by Mats Gustafsson (unpublished data) and the sample was prepared by Harry Saumweber.]

[Eq. 7(a); Gustafsson, 2000; Heintzmann, 2003; Fig. 13.8(E)]. The weights of this averaging in Fourier-space are adjusted as inverse variances of the noise such that the best quality reconstruction at each frequency is preferred over more noisy reconstructions. Finally, there is an inverse Fourier transformation back to real space [Figs. 13.8(F)]. The resolution improvement obtained can be seen in Figure 13.8(K) compared to what is obtained by just adding the widefield detected set of images [Fig. 13.8(H)] even after contrast enhancement [Fig. 13.8(I)] or by processing the same data to simulate confocal imaging [Fig. 13.8(J)]. In Figure 13.9 the resolution improvement is even more obvious. This figure was generated by illumination with a grating close to the highest transmittable spatial frequency, which leads to more prominent high-frequency components with less noise after their extraction (kindly provided by M. G. L. Gustafsson). In some of the figures [especially in Fig. 13.8(I)] a residual patterning can be observed. This can be attributed to having selected too few pattern positions (here  $6 \times 6 = 36$ ) in the set.

It is interesting to note that the sampling of the raw data images need only satisfy the Nyquist limit of the widefield microscope even though the resolution finally achieved extends beyond this limit. During the relocation process of the object components in the reconstruction, the discrete frequency space can be “extended,” essentially resampling the data onto a different grid. This reconstruction does not contradict information theory because many images, each with different high-frequency sample information (but downshifted into the detection pass-band) are used to construct a single image containing information outside the detection passband. Although negative intensities can in principle result

during the process of image reconstruction, this does usually not pose a practical problem.

With this approach, the resolution of the microscope can theoretically be enhanced by a factor of about 2 in-plane ( $xy$ ) as well as along the optic axis ( $z$ ) compared to the standard epifluorescence widefield microscope. Although the fundamental pass-band limit obtained by this method is not larger than the pass-band of a confocal microscope, a substantial practical improvement over standard confocal microscopy is achieved. The high spatial frequencies of the object are detected much more efficiently because the moiré effect of the illumination grid shifts them into a region of the pass-band that is more efficiently detected.

Lucosz’s formulation (Lucosz and Marchand, 1963; Lucosz, 1967) makes it possible to understand both the confocal microscope and multiple dot-scanning systems in the nomenclature of computational reconstruction. The moving detection mask of these systems, in combination with the integration of partial images on the detector, permits the required unmixing to be achieved automatically, the positions of the zero frequencies of the unmixed components to be correctly adjusted and integrated (which means essentially summed) in the detector with component-dependent weights. Thought of in this way, the shape and size of the detection pinhole defines the relative weights of individual object components.

As opposed to Lucosz’ approach or scanning disk systems, in which the decoding is achieved by a detection mask, computational reconstruction is far more flexible. Assume as a gedanken experiment that we illuminate the specimen with an array of bright points and then scan these points over the field of view so that

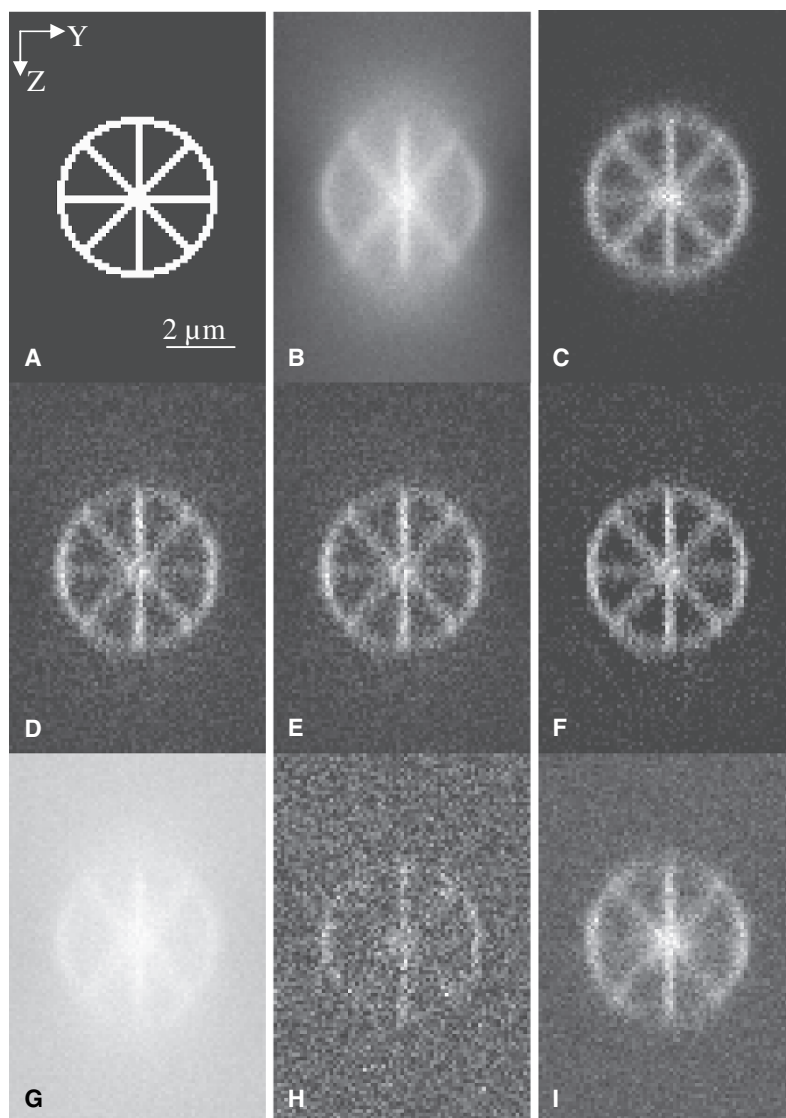


**FIGURE 13.10.** Performance simulation of dense structured illumination for thick samples. (A) Simulated object. (B) Widefield image (1000 expected photons in maximum). (C) Confocal image (pinhole size 0.5 Airy units, detector efficiency 20% that of panel B). (D)  $yz$ -Section computed using Eq. 1 from dense structured illumination, three phases. Further reconstructions were based on (E) Eq. 4, and (F) Eq. 6(b). (G) Widefield image with a background fluorescence added corresponding to approximately five layers of this object when densely packed. (H) Reconstruction (Eq. 4) of a structured-illumination dataset under similar sample conditions. (I) Reconstruction (Eq. 4) of data with the spacing between the illuminating bars increased 3-fold (total illumination dosage was kept constant for all simulations). Simulation parameters as described in the text.

eventually it is all covered. If we record a separate widefield image of the specimen for each location of the excitation array, we now have a stack of data that contains all the information we need to construct an optical section of the focus plane merely by summing the signal collected at virtual “pinholes” near the locations of the excitation points in each image of the stack (similar to the approach chosen for Fig. 13.4). Assuming the same illuminating power, the same scan time, and the same detector performance,<sup>8</sup> this optical section will be in every way identical to one made with a disk-scanning confocal microscope. However, this admittedly rather tedious approach has the added advantage that we could have used any of the seven methods (Eqs. 1–7) for computing optical

<sup>8</sup> Including pixels small enough to accurately delineate the image of each round pinhole in the image of the disk.

sections discussed above and in addition we could compute results to reflect any detector pinhole size after the acquisition of the data.

Although this approaches pure confocal operation (by using very sparse structured illumination), it would be extremely time-consuming to take the many individual images. In addition, taking so many high-speed individual images will increase the readout noise with obvious consequences. Other problems would be caused by the massive amount of data (a full image acquired for each scan position, of which there could be a million). Thus, despite these theoretical advantages, practical limitations still render standard confocal microscopy more useful for imaging thick specimens (for a detailed example, see box “Imaging of Thick Specimens”).

Approaches such as the programmable array microscope (Verveer *et al.*, 1998; Hanley *et al.*, 1999; Heintzmann *et al.*, 2001)

**IMAGING OF THICK SPECIMENS**

In Figure 13.10, a sample consisting of a  $yz$ -oriented star-shaped stack (“wagon-wheel pasta,” see also Chapter 24, *this volume*) and its images were simulated [diameter of object:  $4\ \mu\text{m}$ , voxel size  $100 \times 100 \times 100\ \text{nm}$ , theoretical point spread function of 1.2 NA water immersion ( $n = 1.33$ ) objective. Pattern spacing in sample: (B–H) 900 nm, (I)  $2.7\ \mu\text{m}$ , pattern width 300 nm.] The total dosage delivered to the sample for the acquisition of all of the raw data necessary for panels (B) to (I) was kept constant. This yielded a total of  $1.2 \times 10^6$  detected photons for the central slice (B, D–F),  $28 \times 10^6$  photons (G–I), and  $36 \times 10^3$  photons for the confocal image (C).

The optical sectioning advantage of the confocal (C) over the widefield image (B) is clear even though the signal-to-noise ratio in the confocal image is lower due to rejection of light at the pinhole and lower detection quantum efficiency (QE). Note that in the widefield image only ~17% of the photons in the central slice stem from the in-focus region (3 voxels deep). Images obtained from processing the structured-illumination data (D–F) show only minor differences in quality and are comparable also to the confocal image. However, when additional background is added (as in G, H) stemming from a distant out-of-focus region in the form of five additional densely packed layers of overlying wagon-wheel pasta, the reconstructions from dense three-phase structured-illumination data are of poor quality (H), whereas the confocal image quality (C) would be unaffected. For this amount of background less than 5% of the collected photons stem from the in-focus area.

However, by adjusting the spacing between the illumination bars to yield a more sparse illumination (I), a better sectioning is achieved and the quality of the reconstruction becomes more acceptable. The price of this improvement is that data acquisition takes longer (if limited by the instrument) and the raw data file is larger. By going to even more sparse illumination and a two-dimensional pattern, confocal quality will be reached, but the long acquisition times may be unacceptable. Note that each final reconstruction (including the widefield and confocal cases) assumed that the same total number of photons was emitted by the sample. The confocal detector (photomultiplier tube assumed) was assumed to have a quantum efficiency 20% as high as the detectors used in the widefield detection mode (a good quality CCD assumed). Read noise of the CCD was not accounted for because it would be of marginal influence in these bright images. For a further discussion on the effect of imaging thick specimens see the Appendix of this chapter.

that can rapidly change “pinhole patterns” using a digital mirror device for both illumination and detection, can make use of normally rejected light by sending it to a second detector (Heintzmann *et al.*, 2001) and have obvious advantages in speed and reduction of readout noise in comparison to acquiring all the individual images of a set. However, when integrating over a set of pinhole positions, these devices do not permit the widefield detection of each of the images of a set of structured-illumination data (e.g., changing the pinhole size retrospectively as in Fig. 13.4 is usually not possible).

Computational reconstruction of structured-illumination data is in some ways related to achieving resolution improvement by analysis of a series of intensity distributions at the pinhole plane based on a singular functional decomposition (Bertero *et al.*, 1989), the major difference being that aperture-modifying filters influence the light amplitude and not only the intensity as does reconstruction.

The minimum number of images required is defined by the number of object components that need to be separated [see Figs. 13.6(A) and 13.8(D)]. For a single optical slice, it ranges from three images when using a one-dimensional diffraction grid for improved sectioning (Neil *et al.*, 1997), a low number of images

(typically 7–9) for in-plane resolution improvement with successive rotation of the illumination grid (Heintzmann and Cremer, 1999; Gustafsson, 2000) to many tens of images (Benedetti *et al.*, 1996) for use with relatively sparse two-dimensional patterns (pinhole distance  $\gg$  PSF size).

However, looking at this issue from the perspective of information theory indicates that a reduction of this number should be possible (Cox and Sheppard, 1986). The weighted averaging in the reconstruction process also hints that much of the information has been acquired multiple times. The key to a major reduction in the minimum number of images required is to modify the reconstruction process so that both order separation and weighted averaging are combined into a single processing step (Heintzmann, 2003). When this idea is extended to three-dimensional data, another substantial reduction in the number of images per slice can be expected. For a  $z$ -sectioning image stack using dense grids, this could reduce the minimum to less than three images per slice on average.

When acquiring a focus series (a  $z$ -stack of image sets), the plane of focus for the illumination pattern usually coincides with the plane of focus of the detection path. In this situation, the theory of the imaging process becomes slightly more complex than outlined above. In the description above, the patterns were assumed as being “part of the object,” that is, as its multiplicative modification. However, in  $z$ -direction, patterning has to be treated as being “part of the point spread function” because the illumination pattern usually stays aligned with the plane of best focus as it steps through the sample, and is not fixed to the object.

The standing-wavefield microscope (Bailey *et al.*, 1993; Lanni *et al.*, 1993; Krishnamurthi *et al.*, 1996; So *et al.*, 2001) and the incoherent illumination image interference imaging ( $I^2M$ ) microscope (Gustafsson *et al.*, 1995, 1999) generate patterned illumination with either coherent laser light or an incoherent light source, respectively, and illuminate with alternating bright and dark  $xy$ -planes stacked along the optical axis. In  $I^2M$ , the maximum of the illumination pattern coincides with the plane of best focus in detection. The illumination pattern stays in a fixed spatial relation to the detection point spread function and can thus be treated as part of it. This simplifies the reconstruction, as no computational unmixing is required. However, standing-wavefield microscopy with illumination solely along both directions of the optic axis suffers from a large region of missing intermediate  $z$ -frequencies, essentially rendering three-dimensional reconstruction of large features impossible. (In real space this corresponds to the ambiguity problem between lobes along the  $z$ -axis of the PSF.)

In  $I^2M$ , the situation is much improved, such that it enables image reconstruction (Gustafsson *et al.*, 1999). The effect of noise on  $I^2M$  and 4Pi (which is essentially a point-scanning technique, described in Chapter 30, *this volume*) were compared by Nagorni and Hell (2001a, 2001b) indicating the superior performance of the 4Pi approach, especially along the axial direction. However, a combination of  $I^2M$  with additional patterning along the in-plane directions can be expected to yield an additional increase in resolution. This may also have the potential to overcome some of the signal-to-noise difficulties of  $I^2M$  in comparison to 4Pi microscopy.

All of the reconstruction techniques described above suffer to some extent from photobleaching of the fluorophores. Because bleaching is caused by structured illumination, patterns may be bleached into the sample and have to be compensated for during reconstruction. Efforts to compensate for patterned bleaching are treated in detail by Schaefer and colleagues (2004).

Although the three-dimensional imaging techniques described above have usually been developed for fluorescence, they have

also been applied to incoherent reflection (Neil *et al.*, 1997) and transmission (Dodt *et al.*, 2003). For the coherent case, approaches similar in spirit to the Fourier-techniques developed for synthetic aperture radar are used (Mermelstein, 1999; Schwarz *et al.*, 2003; Nellist *et al.*, 1995).

## Nonlinear Structured Illumination

As described by Heintzmann and colleagues (2002), the methods of structured illumination can be extended to the nonlinear regime of the experiment in a straightforward way, and doing so yields another substantial resolution improvement over linear structured illumination. If any kind of nonlinearity exists between the illumination intensity and the emission intensity finally measured, further peaks in the Fourier-transformation of the effective excitation distribution will arise. In the absence of noise, this allows for any number of components to separate and thus, theoretically, for infinite resolution in the reconstruction. In practice, signal-to-noise issues and the type of nonlinearity limit the achievable resolution, even if grid quality, positioning accuracy, and detector linearity are perfect.

One of the nonlinear effects we have discussed (Heintzmann *et al.*, 2002) is fluorescence saturation (Sandison *et al.*, 1995). In this case, the sample is irradiated with structured illumination over the full field of view. The intensity required to achieve saturation is extremely high, but nevertheless possible by using pulse lasers and illuminating only a few nanoseconds. Recently, this approach has been practically demonstrated by Gustafsson (2005) who claimed an in-plane resolution of  $\sim 50$  nm. This fluorescence saturation idea is related to the saturation of the stimulated emission employed in stimulated emission depletion (STED) microscopy (Klar *et al.*, 2000; see also Chapter 31, *this volume*).

It should be mentioned that multi-focal, two-photon microscopy yields inherent sectioning due to the two-photon effect and thus does not require a detection mask (see also Chapter 29, *this volume*; Andresen *et al.*, 2001). As these systems that illuminate with a pattern of light could allow the detection of the image at every pattern position, the reconstruction technique described above should also be applicable, with its potential for flexibility and resolution improvement. If one neglects the extra readout noise associated with recording all those images, a reconstruction based on such a set of structured-illumination images would increase the signal-to-noise ratio especially for high frequencies in comparison to just acquiring the summed images, as would be done in the standard system. However, because the excitation probability using the two-photon effect is proportional to the square of the incident intensity, analyzing the data as a case of structured illumination would contribute a factor of 2 increase in resolution from the excitation side of the scheme. This would compensate for the longer excitation wavelength used for two-photon excitation. Thus structured illumination based on the nonlinear two-photon effect leads to no major resolution increase compared to single-photon structured illumination. Other nonlinear effects, such as saturation phenomena, do have higher orders, which can also be utilized for substantial resolution improvements (such as in stimulated emission depletion microscopy).

As any type of nonlinearity can be used in combination with this concept, the nonlinearities considered in Hell and Kroug (1995) and Schönle and co-workers (1999) are also promising approaches for the concept described by Heintzmann and Cremer (1999b) and Heintzmann and colleagues (2002). Other extremely promising candidates are dyes (Corrie *et al.*, 2001; Giordano *et al.*, 2002) or proteins (Ando *et al.*, 2004) that can be converted

between two (or multiple) states under wavelength selective illumination. These compounds constitute multi-level systems in which saturation characteristics can be utilized without requiring excessive illumination intensities (Hell, 2004).

## SUMMARY

- Structured illumination in combination with widefield detection typically requires the acquisition of a large amount of data in comparison to standard confocal or Nipkow-type disk systems.
- One need not select a “pinhole size” during data acquisition. The data acquired can be processed in different ways to emphasize different contrast and resolution/noise trade-offs. Depending on the nature of the pattern employed, a practical resolution improvement of a factor slightly above 2 in each direction of space can be achieved compared to standard wide-field microscopy. Using nonlinear approaches this factor can be made substantially bigger.
- Practical speed limits are imposed by the current camera and readout technology, but, more important, by the absence of bright light sources suitable for incoherent full-field illumination.

## ACKNOWLEDGMENTS

Drs. James Pawley, Stefan Höppner, David Richards, Stefan Hell, Thomas Jovin, Anje Sporberr, Verena Hafner, and Keith Lidke are thanked for their help in improving this manuscript. I am very thankful to Dr. Pier Alberto Benedetti, who contributed experimental image data (Fig. 13.8) as did Drs. Bauch, Kempe, Schadwinkel, and Schaffer (Fig. 13.7) from Carl Zeiss, Göttingen, Germany. Furthermore, Drs. Thomas Jovin, Christoph Cremer, Mats Gustafsson, Stefan Hell, Jan Boese, and Quentin Hanley are thanked for many fruitful discussions regarding patterned illumination.

## REFERENCES

- Andresen, V., Egner, A., and Hell, S.W., 2001, Time-multiplexed multifocal multiphoton microscope, *Opt. Lett.* 26:75–77.
- Ando, R., Mizuno, H., and Miyawaki, A., 2004, Regulated fast nucleocytoplasmic shuttling observed by reversible protein highlighting, *Science* 306:1370–1373.
- Barth, M., and Stelzer, E.H.K., 1994, Boosting the optical transfer-function with a spatially resolving detector in a high numerical aperture confocal reflection microscope, *Optik* 96:53–58.
- Bailey, B., Farkas, D.L., Taylor, D.L., and Lanni, F., 1993, Enhancement of axial resolution in fluorescence microscopy by standing wave excitation, *Nature* 366:44–48.
- Ben-Levy, M., and Peleg, E., August 1995, WO 97/06509, US Patent 5,867,604.
- Benedetti, P.A., Evangelista, V., Guidarini, D., and Vestri, S., 1996, US Patent 6,016,367.
- Bertero, M., Boccacci, P., Defrise, M., De Mol, C., and Pike, E.R., 1989, Super-resolution in confocal scanning microscopy: II. The incoherent case, *Inverse Problems* 5:441–461.
- Bertero, M., De Mol, C., Pike, E.R., and Walzer, J.G., 1984, Resolution in diffraction-limited imaging, a singular value analysis. IV. The case of uncertain localization or non-uniform illumination of the object. *Opt. Acta* 31:923–946.
- Bewersdorf, J., Pick, R., and Hell, S.W., 1998, Multifocal multiphoton microscopy, *Opt. Lett.* 23:655–657.

- Corrie, J.E., Davis, C.T., and Eccleston, J.F., 2001, Chemistry of sulforhodamine-amine conjugates, *Bioconjug. Chem.* 12:186–194.
- Cox, I.J., and Sheppard, C.J.R., 1986, Information capacity and resolution in an optical system, *J. Opt. Soc. Am. A* 3:1152–1158.
- Dotz, H.-U., 1990, German Patent DE 40 23 650 A1.
- Dotz, H.-U., and Becker, K., 2003, Confocal microscopy in transmitted light, *Proc. SPIE* 5139:79–87.
- Dotz, H.-U., Becker, K., Eder, M., and Zieglgänsberger, W., 2001, Confocal microscopy of unstained neurons in brain slices, *Schloessmann Seminar 2001 Abstractbook*, Max-Planck Society, Schloss Elman, Oberbayern, DE, pp. 22–23.
- Egner, A., Jakobs, S., and Hell, S.W., 2002, Fast 100-nm resolution 3D-microscope reveals structural plasticity of mitochondria in live yeast, *Proc. Natl. Acad. Sci. USA* 99:3370–3375.
- Failla, A.V., Spoeri, U., Albrecht, B., Kroll, A., and Cremer, C., 2002, Nanosizing of fluorescent objects by spatially modulated illumination microscopy, *Appl. Opt.* 41:7275–7283.
- Frohn, J.T., Knapp, H.F., and Stemmer, A., 2000, True optical resolution beyond the Rayleigh limit achieved by standing wave illumination, *Proc. Natl. Acad. Sci. USA* 97:7232–7236.
- Frohn, J.T., Knapp, H.F., and Stemmer, A., 2001, Three-dimensional resolution enhancement in fluorescence microscopy by harmonic excitation, *Opt. Lett.* 26:828–830.
- Fukano, T., and Miyawaki, A., 2003, Whole-field fluorescence microscope with digital micromirror device: Imaging of biological samples, *Appl. Opt.* 42:4119–4124.
- Giordano, L., Jovin, T.M., Irie, M., and Jares-Erijman, E.A., 2002, Diheteroarylethenes as thermally stable photoswitchable acceptors in photochromic fluorescence resonance energy transfer (pcFRET) *J. Am. Chem. Soc.* 124:7481–7489.
- Gustafsson, M.G.L., 2000, Surpassing the lateral resolution limit by a factor of two using structured illumination microscopy, *J. Microsc.* 198:82–87.
- Gustafsson, M.G.L., 2005, Non-linear structured-illumination microscopy: widefield fluorescence imaging with theoretically unlimited resolution, *Proc. Nat. Acad. Sci. USA* 102:13081–13086.
- Gustafsson, M.G.L., Agard, D.A., and Sedat, J.W., 1999, F<sup>3</sup>M: 3D widefield light microscopy with better than 100 nm axial resolution, *J. Microsc.* 195: 10–16.
- Gustafsson, M.G.L., Agard, D.A., and Sedat, J.W., 2000, Doubling the lateral resolution of widefield fluorescence microscopy using structured illumination microscopy, *Proc. SPIE* 3919:141–150.
- Gustafsson, M.G.L., Sedat, J.W., and Agard, D.A., US Patent 5,671,085.
- Hanley, Q.S., Verwee, P.J., Gemkov, M.J., Arndt-Jovin, D., and Jovin, T.M., 1999, An optical sectioning programmable array microscope implemented with a digital micromirror device, *J. Microsc.* 196:317–331.
- Heintzmann, R., 2003, Saturated patterned excitation microscopy with two-dimensional excitation patterns, *Micron* 34:283–291.
- Heintzmann, R., and Cremer, C., 1999a, Laterally modulated excitation microscopy: improvement of resolution by using a diffraction grating, *Proc. SPIE* 3568:185–196.
- Heintzmann, R., and Cremer, C., March 1999b, Patent WO 0052512.
- Heintzmann, R., Jovin, T.M., and Cremer, C., 2002, Saturated patterned excitation microscopy — a concept for optical resolution improvement, *J. Opt. Soc. Am. A* 19:1599–1609.
- Heintzmann, R., Hanley, Q.S., Arndt-Jovin, D., and Jovin, T.M., 2001, A dual path programmable array microscope (PAM): Simultaneous acquisition of conjugate and non-conjugate images, *J. Microsc.*, 204:119–137.
- Hiraoka, Y., Sedat, J.W., and Agard, D.A., 1990, Determination of 3-dimensional imaging properties of a light-microscope system — partial confocal behaviour in epifluorescence microscopy, *Biophys. J.* 57:325–333.
- Hell, S.W., 2004, Strategy for far-field optical imaging and writing without diffraction limit, *Phys. Lett. A* 326:140–145.
- Hell, S.W., and Kroug, M., 1995, Ground-state depletion fluorescence microscopy, a concept for breaking the diffraction resolution limit, *Appl. Phys. B* 60:495–497.
- Ichihara, A., Tanaami, T., Isozaki, K., Sugiyama, Y., Kosugi, Y., Mikuriya, K., Abe, M., and Uemura, I., 1996, High-speed confocal fluorescence microscopy using a Nipkow scanner with microlenses for 3-D imaging of single fluorescent molecules in real time, *Bioimages* 4:57–62.
- Klar, T.A., Jakobs, S., Dyba, M., and Hell, S.W., 2000, Fluorescence microscopy with diffraction resolution barrier broken by stimulated emission, *Proc. Natl. Acad. Sci. USA* 97:8206–8210.
- Krishnamurthi, V., Bailey, B., and Lanni, F., 1996, Image processing in 3D standing-wave fluorescence microscopy, *Proc. SPIE* 2655:18–25.
- Lanni, F., Bailey, B., Farkas, D.L., and Taylor, D.L., 1993, Excitation field synthesis as a means for obtaining enhanced axial resolution in fluorescence microscopes, *Bioimaging* 1:187–196.
- Lanni, F., Taylor, D.L., and Waggoner, A.S., 1986, US Patent 4,621,911.
- Lukosz, W., 1967, Optical systems with resolving powers exceeding the classical limit. II, *J. Opt. Soc. Am.* 57:932–941.
- Lukosz, W., and Marchand, M., 1963, Optischen Abbildung unter Überschreitung der beugungsbedingten Auflösungsgrenze [in German], *Opt. Acta* 10:241–255.
- Majoul, I., Straub, M., Duden, R., Hell, S. W., and Söling, H. D., 2002, Fluorescence resonance energy transfer analysis of protein-protein interactions in single living cells by multifocal multiphoton microscopy, *Rev. Mol. Biotechnol.* 82:267–277.
- Mermelstein, M.S., 1999, Synthetic aperture microscopy, Ph.D. thesis, Massachusetts Institute of Technology, Cambridge, MA, June 1999.
- Nagorni, M., and Hell, S.W., 2001a, Coherent use of opposing lenses for axial resolution increase in fluorescence microscopy. I. Comparative study of concepts, *J. Opt. Soc. Am. A* 18:36–48.
- Nagorni, M., and Hell, S.W., 2001b, Coherent use of opposing lenses for axial resolution increase. II. Power and limitation for nonlinear image restoration, *J. Opt. Soc. Am. A* 18:49–54.
- Neil, M.A.A., Juskaitis, R., and Wilson, T., 1997, Method of obtaining optical sectioning by using structured light in a conventional microscope, *Opt. Lett.* 22:1905–1907.
- Nellist, P.D., McCallum, B.C., and Rodenburg, J.M., 1995, Resolution beyond the “information limit” in transmission electron microscopy, *Nature* 374:630–632.
- Pawley, J., Blouke, M., and Jenesick, J., 1996, The CCDiode: An optimal detector for laser confocal microscopes, *Proc. SPIE* 2655:125–129.
- Petráň, M., Hadravsky, M., Egger, M.D., and Galambos, R., 1968, Tandem-scanning reflected-light microscope, *J. Opt. Soc. Am.* 58:661.
- Sandison, D.R., Williams, R.M., Wells, K.S., Strickler, J., and Webb, W.W., 1995, Quantitative fluorescence confocal laser scanning microscopy (CLSM), In: *Handbook of Biological Confocal Microscopy*, 2nd ed. (J.B. Pawley, ed.), Plenum Press, New York, pp. 267–268.
- Schaefer, L.H., Schuster, D., and Schaffer, J., 2004, Structured illumination microscopy: artefact analysis and reduction utilizing a parameter optimization approach, *J. Microsc.* 216:165–174.
- Schönle, A., Hänninen, P.E., and Hell, S.W., 1999, Nonlinear fluorescence through intermolecular energy transfer and resolution increase in fluorescence microscopy, *Ann. Phys. (Leipzig)* 8:115–133.
- Schwarz, C.J., Kuznetsova, Y., and Brueck, S.R.J., 2003, Imaging interferometric microscopy, *Opt. Lett.* 28:1424–1426.
- Sheppard, C.J.R., and Cogswell, C.J., 1990, Confocal microscopy with detector arrays, *J. Modern Opt.* 37:267–279.
- So, P.T.C., Kwon, H-S., and Dong, C.Y., 2001, Resolution enhancement in standing-wave total internal reflection microscopy: a point-spread-function engineering approach, *J. Opt. Soc. Am. A* 18:2833–2845.
- Verwee, P.J., Hanley, Q.S., Verbeek, P.W., van Vliet, L.J., and Jovin, T.M., 1998, Theory of confocal fluorescence imaging in the programmable array microscope (PAM), *J. Microsc.* 189:192–198.
- Wilson, T., Juskaitis, R., Neil, M.A.A., and Kozubek, M., 1996, Confocal microscopy by aperture correlation *Opt. Lett.* 21:1879–1881.
- Yaroslavsky, L., 2003, Boundary effect free and adaptive discrete signal sinc-interpolation algorithms for signal and image resampling, *Appl. Opt.* 42:4166–4175.

## APPENDIX: IMAGING THICK SPECIMEN WITH STRUCTURED ILLUMINATION

What illumination pattern do we choose for what specimen? If we neglect issues of resolution, it is apparent that a very thin sample (e.g., single molecules diffusing in a flat biomembrane) can be imaged with full-field illumination and widefield detection, whereas a very thick sample, containing a lot of fluorophores (e.g., a fish embryo expressing green fluorescent protein (GFP) throughout all the cells) requires confocal imaging. Widefield imaging has the advantage of being relatively fast and efficient in signal detection. Confocal imaging allows for the rejection of the “bad,” that is, unemployable out-of-focus light that would dominate the signal in full-field illumination.

Structured illumination with a user-defined illumination pattern covers the entire range from full-field illumination through dense illumination patterns to sparse illumination, approximating single-spot confocal illumination conditions.

The crucial task is to obtain an estimate of the noise level that we should expect in the final data with different illumination patterns.

If we first assume full-field illumination with the fraction of the illumination area, the mark/area ratio  $MAR = 1$ , each horizontal plane will be illuminated with the same intensity, independent of its axial position. Depending on the structure of the sample, a defined thickness  $Z_{eq}$  will yield an equal amount of foreground signal and out-of-focus haze. Structured-illumination techniques and even widefield deconvolution aim at computationally removing this out-of-focus haze. However, although background removal (e.g., by subtraction) can be achieved, the noise contribution of the background to the signal will still be present. Thus, specimens considerably thicker than  $Z_{eq}$  (e.g., more than 10 times as thick) will run into signal-to-noise problems (see discussion below).

Consider now an illumination pattern of horizontal bars of a thickness of  $d = 5 \mu\text{m}$  with a pitch (distance between the beginning of one bar and the beginning of the next bar) of  $D = 50 \mu\text{m}$ .

The mark/area ratio is defined as  $MAR = \frac{d}{D} = \frac{1}{10}$  which is related

to the mark/space ratio by  $MSR = \frac{d}{D-d} = \frac{1}{\frac{1}{MAR} - 1}$ . If these

bars are sufficiently wider than the diffraction limit, such that diffraction effects can be neglected, structured illumination allows the acquisition of the foreground in full brightness (knowing which parts of the in-focus slice are illuminated) while reducing the out-of-focus haze by the mark/area ratio.

When an in-focus structure of interest is not illuminated, which in this case happens in 90% of the images acquired in each set of frames, the background described above is still present. However, it can be assumed that the reconstruction algorithm can account for this foreground region not being illuminated because it knows the current illumination structure and uses this information merely for a precise estimate<sup>9</sup> of the amount of background. This estimate is then successively removed from the “foreground” data, acquired when the particle was illuminated (e.g., using Eqs. 6a and 6b).

In the discussion above, it is assumed that out-of-focus light only influences the result as if it were detected as an additional, local uniform background (with its associated Poisson noise), and that a uniform illumination applies even to fluorophores situated directly behind or in front of the plane of focus. This is clearly NOT true for the patterned illumination geometry given in Figure 13.11(B). The parameters  $d$  and  $D$  define three illumination/detection regimes depending on whether the fluorescent structure is *in focus*, *close*, or *distant* from the focus plane. These regimes are characterized as follows:

- **In focus:** In this refined model, diffraction effects will blur the thin-line illumination, reducing its intensity. As a result, “background” contributions will arise from neighboring regions where illumination was not intended. These in-plane “spill-over” effects are approximated in an *ad hoc* way by the following in-focus contrast reduction factor of the foreground:

$$\text{contrast} = d_{\text{rel}} / (d_{\text{rel}} + \epsilon),$$

where  $d_{\text{rel}} = d/d_{\text{min}}$  is the width of a bar compared to the smallest transmittable spatial wavelength of the objective at the emission wavelength  $d_{\text{min}} = \lambda_{\text{em}} / (2NA)$ .

The number,  $\epsilon = 1.828$  was fitted from a simulation of the image of a bar with variable width at  $NA = 1.4$ .

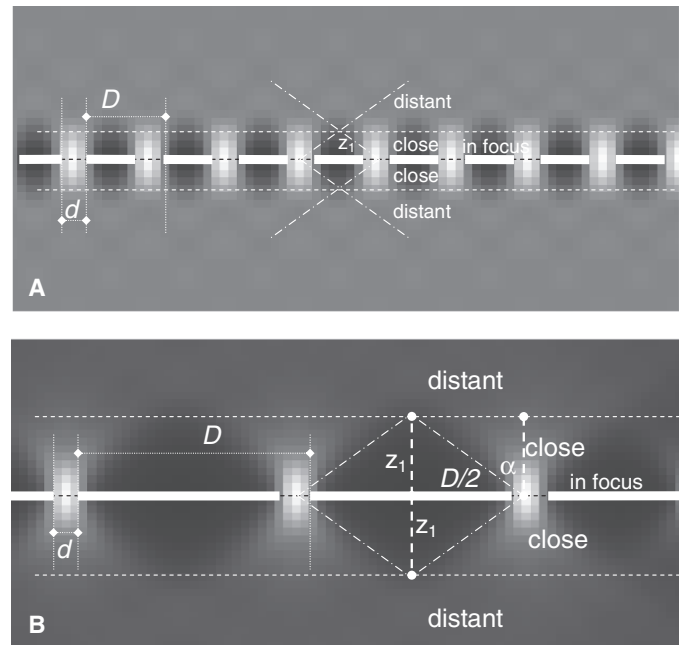


**FIGURE 13.11.** Background in thick samples. The sample is assumed to resemble a “sea” of fluorescence. The image depicts the illumination brightness distribution in the sample, viewed from the side. The fraction of emitted light from a specific plane falling on the illuminated grid-pattern geometric positions is also proportional to this distribution, which has to be integrated over a full unit-cell (here distance  $D$ ). The region very close to the illuminating bars or squares should start with a widefield-like behavior. However, to keep the model simple the whole region from the bars to the *distant* region is denoted *close* in which a linear decay in the background stemming from an out-of-focus plane, detected at the nominally illuminated in-focus positions. Note the difference for dense (A) and sparse illumination (B) corresponding to the simulations shown in Figure 13.10.

<sup>9</sup> The quality of this estimate is better by a factor of  $\sqrt{\frac{1}{MAR} - 1} = 3$  than the signal, thus exhibiting only 1/3 of the noise.

- **Close** [ $0 < z \leq z_1 = D/(2 \tan \alpha)$ ]: Transition occurs between in-focus illumination and detection and dimmed-field scaling. This simplified model assumes a linear transition between the foreground in the *in-focus* slice and the background contributions in each plane of the *distant* region.
- **Distant** ( $z_1 < z$ ): Dimmed-field scaling. Above the distance  $z_1 = D/(2 \tan \alpha)$  from the plane of focus, all contributing background is assumed to be illuminated evenly as assumed in the discussion above. In contrast to the *in-focus* regime, features in this region receive illumination intensity dimmed by the mark/area ratio (MAR).

In Figure 13.12 the relative contribution of a planar fluorescent sheet at a defined distance from the plane of focus to the illuminated in-focus pixels is shown (simulation on a  $400 \times 400$  pixel grid, pixel size 60 nm, at 520 nm, NA = 1.2 and water immersion  $n = 1.33$ ). The simplified theory agrees reasonably well with the detailed simulation (with emission wavelength 520 nm, NA = 1.2, water immersion with refractive index  $n = 1.33$ ). Here the MAR was kept constant as  $1/4$  (e.g., as it could be in an ApoTome) and

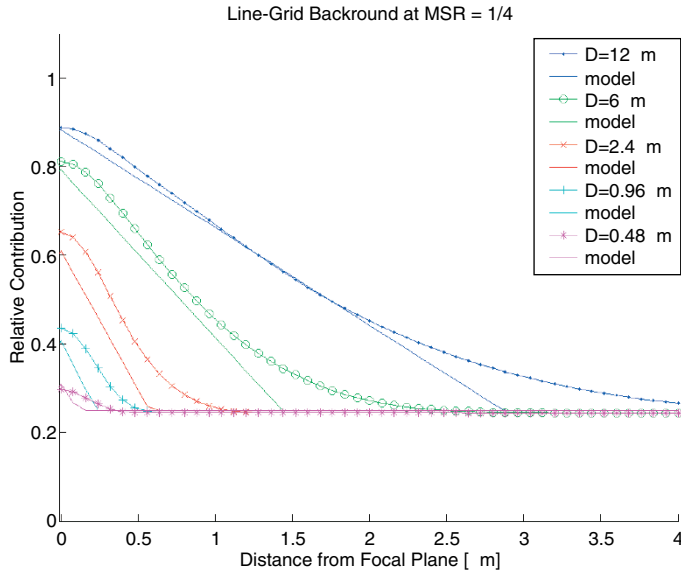


**FIGURE 13.12.** Comparison of rough model (from Fig. 13.11) with detailed calculations at  $MAR = 1/4$ . (A) Shown is the relative contribution each plane of focus makes to the signal detectable in the geometric position of the bars used for illumination. The “model” curves are calculated according to the approximations shown in Figure 13.11, the contribution of each plane to the background drops linearly (*close* regime) to reach a relative level of  $MAR = d/D$  at distances bigger than  $z_1$  (*distant* regime).

the pitch and width of the bars were varied synchronously. As the width of the bars gets smaller, the foreground signal decreases. It is interesting to note that, for samples of relatively small depth, there is an optimal illumination pattern that provides the best signal-to-noise ratio. For thicker samples, the initial curve shape can be neglected as long as the width of the bars is well above the diffraction limit. The maximal achievable thickness then scales reciprocally with the chosen MAR as in the simplified initial model.

Similar simulations performed for two-dimensional patterns, revealed that the model can safely be extended in an *ad hoc* way by assuming the out-of-focus contributions to be described by a product of the results from the appropriate line grids (even though the problem is, strictly speaking, not separable).

### Dependence of the Maximal Sample Thickness on the Number of Collected Photons

Let us assume that a total of 1000 photons/pixel are detected from a feature during the collection of as many images as are needed to illuminate the entire plane. In other words, if the dark space becomes larger, more exposures are needed to illuminate the entire plane but exposure must now involve fewer photons. Problems arise, if the foreground (1000 photons) cannot be distinguished from the noise of the total signal  $s = fg + bg$  (sum of background  $bg$  and foreground  $fg$ ). The noise scales with the square root of  $s$ . To achieve a defined signal-to-noise ratio ( $S/N$ ) for the foreground-only signal ( $fg^{rec}$ ) reconstructed by subtracting the background (here assumed to be estimated perfectly), we obtain:

$$S/N = \frac{fg^{rec}}{\text{noise}(fg^{rec})} = \frac{fg}{\sqrt{fg + bg}}, \text{ thus } bg = \left( \frac{fg}{S/N} \right)^2 - fg, \text{ which}$$

is the maximum acceptable background level given the specified foreground level (in photons) and the required signal-to-noise ratio. Assuming a signal-to-noise ratio of 10 gives reasonable image quality, and assuming essentially noise-free background estimation, the background level  $bg$  in the raw data can be as high as 9000 photons/pixel (i.e., the background signal can be ~9 times higher than the foreground). However, if only 200 photons can be collected from the foreground object, the background cannot go above 200 photons without dropping the  $S/N$  below 10.

Therefore, two effects determine the maximum sample thickness. The structure of the illumination pattern will define the break-even distance  $Z_{eq}$  at which the out-of-focus haze equals the foreground. The number of collected photons from the structure of

interest then finally determines the factor  $\gamma = \frac{fg}{S/N^2} - 1$  by which the sample thickness can exceed  $Z_{eq}$ , while still maintaining a signal-to-noise ratio above the given limit ( $S/N$ ).